

# Coupling hydrodynamics with comoving frame radiative transfer

## II. Stellar wind stratification in the high-mass X-ray binary Vela X-1

A. A. C. Sander<sup>1</sup>, F. Fürst<sup>2</sup>, P. Kretschmar<sup>2</sup>, L. M. Oskinova<sup>1</sup>, H. Todt<sup>1</sup>, R. Hainich<sup>1</sup>, T. Shenar<sup>1</sup>, and W.-R. Hamann<sup>1</sup>

<sup>1</sup> Institut für Physik und Astronomie, Universität Potsdam, Karl-Liebknecht-Str. 24/25, D-14476 Potsdam, Germany  
e-mail: ansander@astro.physik.uni-potsdam.de

<sup>2</sup> European Space Astronomy Centre (ESA/ESAC), Science Operations Department, Villanueva de la Cañada (Madrid), Spain

Received <date> / Accepted <date>

### ABSTRACT

*Context.* Vela X-1, a prototypical high mass X-ray binary (HMXB), hosts a neutron star (NS) in a close orbit around an early B-supergiant donor star. Accretion of the donor star's wind onto the NS powers its strong X-ray luminosity. To understand the physics of HMXBs, detailed knowledge about the donor star winds is required.

*Aims.* To gain a realistic picture of the donor star in Vela X-1, we construct a hydrodynamically consistent atmosphere model describing the wind stratification while properly reproducing the observed donor spectrum. To investigate how X-ray illumination affects the stellar wind, we calculate additional models for different X-ray luminosity regimes.

*Methods.* We use the recently updated version of the PoWR code to consistently solve the hydrodynamic equation together with the statistical equations and the radiative transfer.

*Results.* The wind flow in Vela X-1 is driven by ions from various elements with Fe III and S III leading in the outer wind. The model-predicted mass-loss rate is in line with earlier empirical studies. The mass-loss rate is almost unaffected by the presence of the accreting neutron star in the wind. The terminal wind velocity is confirmed at  $v_\infty \approx 600 \text{ km s}^{-1}$ . On the other hand, the wind velocity in the inner region where the NS is located is only  $\approx 100 \text{ km s}^{-1}$ , which is not expected on the basis of a standard  $\beta$ -velocity law. In models with an enhanced level of X-rays, the velocity field in the outer wind can be altered. If the X-ray flux is too high, the acceleration breaks down due to increased ionization.

*Conclusions.* Accounting for radiation hydrodynamics, our Vela X-1 donor atmosphere model reveals a low wind speed at the NS location, and provides quantitative information on wind driving in this important HMXB.

**Key words.** Stars: mass-loss – Stars: winds, outflows – Stars: early-type – Stars: atmospheres – Stars: massive – X-rays: binaries

### 1. Introduction

High mass X-ray binaries (HMXBs) consist of a compact object – either a neutron star or a black hole – accreting material from a massive donor star. As such they are a unique link between different important astrophysical fields, combining high-energy astrophysics and accretion with stellar outflows and winds. An especially interesting subclass of HMXBs are the so-called “wind-fed” systems where the compact object accretes material directly from the stellar wind of the donor. (See Martínez-Núñez et al. 2017, for a recent review on this subclass.) The prototype of such systems is Vela X-1, discovered by Chodil et al. (1967) with its B-supergiant donor HD 77581. To avoid confusion, we will hereafter refer to the system as Vela X-1, stating explicitly if the donor star or the neutron star are being referred to wherever necessary. The adopted parameters for the Vela X-1 system used or discussed throughout this work are compiled in Table. 1.

Vela X-1 is a persistent X-ray source with a typical luminosity a few times  $10^{36} \text{ erg s}^{-1}$ . The X-ray source displays significant variability including bright flares and very low, or “off” states (e.g. Kreykenbohm et al. 2008; Martínez-Núñez et al. 2014). Vela X-1 is an eclipsing binary providing a rare opportunity to study the wind of donor star during the X-ray eclipse. Observations of the system during the eclipse with various instruments (Sato et al. 1986; Nagase et al. 1994; Sako et al. 1999; Schulz et al. 2002) provide evidence for the presence of optically

thick and clumped matter in addition to warm ionized plasma. The mean flux and variability are explained by accretion from a wind with a complex structure, including clumps, turbulent motion and larger structures (e.g. Fürst et al. 2010; Manousakis & Walter 2015). A precise knowledge about the donor star and its wind parameters is essential to study these hypotheses in detail and understand wind-fed HMXBs in general.

The X-ray variability of Vela X-1 has recently been modeled by Manousakis & Walter (2015) using the 2D hydrodynamics code VH-1 (Blondin et al. 1990, 1991; Blondin & Pope 2009). Such elaborated, multi-dimensional hydrodynamics codes allow for complex geometries, but they treat the donor wind in an approximate way, e.g. by using the Sobolev approximation of a CAK radiative force (Castor et al. 1975; Blondin et al. 1990) and an ionization parameter  $\xi$ . On the other hand, sophisticated stellar atmosphere models allow for a detailed study of the line-driven donor wind, accounting for a variety of elements with a multitude of levels and a detailed radiative transfer without assuming a local thermodynamical equilibrium (non-LTE). However, such sophisticated model stellar atmospheres are restricted to a one-dimensional description. Therefore, both approaches, multi-D hydrodynamic models and sophisticated stellar atmosphere models are truly complementary.

The donor wind of Vela X-1 was recently analyzed by Giménez-García et al. (2016), using for the first time state-of-the-art expanding stellar atmosphere models for radiatively-

**Table 1.** Selected Vela X-1 system parameters used or discussed throughout this work

Parameter	Value	Ref./Note
$P_{\text{orb}}$ [days]	8.964357	(1)
$e$	0.0898	(2)
$d_{\text{NS}}$ [cm]	$3.5 \cdot 10^{12}$	(3)
$v_{\text{rot}} \cdot \sin i$ [km s $^{-1}$ ]	56	(4)
$v_{\text{orb}}$ [km s $^{-1}$ ]	284	(a)

**Notes.** <sup>(1)</sup> Kreykenbohm et al. (2008) <sup>(2)</sup> Bildsten et al. (1997) <sup>(3)</sup> Giménez-García et al. (2016) <sup>(4)</sup> Fraser et al. (2010) <sup>(a)</sup> calculated from  $P_{\text{orb}}$  and  $d_{\text{NS}}$ , assuming a circular orbit

driven winds. Their results provided important hints on a potential dichotomy between wind properties in classical persistent supergiant X-ray binaries (SGXBs) and the so-called supergiant fast X-ray transients (SFXTs) that exhibit a significant variation of their X-ray luminosity between quiescence and outbursts.

The models used in Giménez-García et al. (2016) were using a prescribed wind velocity field, and hence were measuring precisely only the terminal wind velocity  $v_{\infty}$ . However, more important in terms of accretion onto a NS is of course the wind velocity at the location of the neutron star  $d_{\text{NS}}$ . For Vela X-1, van Kerkwijk et al. (1995) determined  $d_{\text{NS}} \sim 53 R_{\odot}$  or  $\sim 1.8 R_*$  at periastron, a relatively common value for such systems (e.g. Falanga et al. 2015).

In these cases, where the neutron star is only about a stellar radius away from the donor, we have  $v(d_{\text{NS}}) \ll v_{\infty}$  and thus  $v(d_{\text{NS}})$  depends significantly on the shape of the velocity field. Current state-of-the-art stellar atmospheres normally do not have a self-consistent wind stratification, but instead assume a stratification given by a so-called  $\beta$ -law, i.e.

$$v(r) = v_{\infty} \left( 1 - \frac{R_*}{r} \right)^{\beta}. \quad (1)$$

While this is usually sufficient to measure the stellar and wind parameters quite accurately, it essentially means that in such models the balance between inward and outward pushing forces is usually violated and one would not actually obtain the assumed velocity field when solving the hydrodynamic equation of motion, which we will simply refer to as the “hydrodynamic equation” for convenience. In a lot of applications this is not necessary. However, as soon as one is not only interested in the global stellar and wind parameters, but instead in the particular physical properties throughout the stratification, especially closer to the star, the use of such an approximate treatment can lead to significant errors in the deduced properties. To overcome this problem, we present a hydrodynamically self-consistent atmosphere model for the donor of Vela X-1, using the recent method presented in Sander et al. (2017) for a new generation of models developed with the Potsdam Wolf-Rayet (PoWR) code.

A comparable approach has been used by Krtićka et al. (2012) who calculated a set of 1D wind models for different orbit inclination angles. This and their followed-up work focused on either the angle-dependent behavior and a parameter-space study (Krtićka et al. 2015), while stellar parameters were adopted from previous literature and no spectral cross-check of the results was performed. In this work, we focus on obtaining a hydrodynamically self-consistent solution for wind structure and comparing our results with the observed optical/UV spectra. The goal is to obtain a detailed wind stratification tailored for the Vela X-1 donor.

This approach allows us to check whether the relatively low value of  $v_{\infty} \approx 700 \text{ km s}^{-1}$  measured by Giménez-García et al. (2016) can be explained by radiative driving only, or if additional mechanisms have to be taken into account, such as e.g. the influence of X-ray irradiation of the donor wind. Furthermore, we can qualitatively mimic the orbital modulation of the UV wind lines as originally predicted by Hatchett & McCray (1977) and compare the model with observations to gain further insight on the wind structure. In this paper we present hydrodynamically consistent stellar atmosphere solutions for three test cases and also provide the resulting wind stratifications especially for the potential use in further studies.

In Sect. 2 we give a brief overview of the physics applied in the PoWR models used in this work. The following Sect. 3 then discusses the results of the modeling with subsections focusing on the differences compared to the model from Giménez-García et al. (2016) using a prescribed mass-loss rate and velocity field, a study if the X-ray influence and the discussion of the wind driving and the particular effect of the X-rays on it for the Vela X-1 donor. Finally, the conclusions are drawn in Sect. 4.

## 2. PoWR

### 2.1. Fundamental concepts and parameters

The Potsdam Wolf-Rayet (PoWR) model atmosphere code (e.g. Gräfener et al. 2002; Hamann & Gräfener 2003; Sander et al. 2015) allows to calculate stellar atmosphere models for a spherically symmetric star with a stationary mass outflow. The intricate non-LTE conditions in such atmospheres are properly accounted for by performing the radiative transfer in the co-moving frame and obtaining the population numbers from the equations of statistical equilibrium. As these two are highly coupled, they are iteratively updated together with the electron temperature stratification. The latter is required to ensure energy conservation in the expanding atmosphere and can be obtained with the improved Unsöld-Lucy method described in Hamann & Gräfener (2003) or alternatively via the electron thermal balance (see Sander et al. 2015, and references therein). In the parameter regime used in this work, the electron thermal balance combined with the flux consistency terms from the Unsöld-Lucy method turned out to be most effective in order to gain a stable and reliable temperature stratification.

Following the empirical solution for the Vela X-1 donor by Giménez-García et al. (2016), we define our PoWR models used in this work via the following basic input parameters: The stellar temperature ( $T_*$ ) at a radius where the Rosseland continuum optical depth is  $\tau_{\text{Ross}} = 20$ , the luminosity ( $L$ ), and the stellar mass ( $M_*$ ). The stellar radius  $R_*$  is then defined via the Stefan-Boltzmann law ( $L = 4\pi\sigma_{\text{SB}}T_*^4R_*^2$ ) and the surface gravity  $g_* = g(R_*)$  immediately follows from  $g_* = GM_*R_*^{-2}$ . A full list of possible input parameter combinations for PoWR models is given in Sander et al. (2017).

Density inhomogeneities can be accounted for in the form of optically thin clumps with a void interclump medium and described by density contrast  $D(r)$ . As suggested by the notation, the density contrast can be depth-dependent. Various depth-dependent parametrizations exist and since their different effects could easily give rise to a paper of its own, we will stick to one of them for all hydrodynamically consistent models used throughout this work. In our case we use a similar approach as for the O supergiant model in Sander et al. (2017), namely  $D(r) = 1/f_V(r)$

with

$$f_V(r) = f_{V,\infty} + (1 - f_{V,\infty}) \cdot \exp\left(-\frac{\tau_{cl}}{\tau_{Ross}(r)}\right), \quad (2)$$

i.e. we assume an essentially unclumped atmosphere at the inner boundary with a smooth transition to a significantly clumped wind in the outer part. The parameter  $\tau_{cl}$ , which is set to 0.1 in this work unless otherwise noted, does not mark a strict transition zone but instead describes a characteristic value for the (noticeable) onset of the clumping. The maximum value of  $D_\infty = 11$  is taken from Giménez-García et al. (2016). They did not use Eq. (2), but a different clumping parametrization with two velocities describing the region where the clumping factor increases. Unfortunately, a parametrization connecting density contrasts with explicit velocities is numerically unfavorably in the case of updates of  $v(r)$ , which is why we changed to Eq. (2) for this work.

For a converged atmosphere model, the synthetic spectrum is calculated using a formal integration in the observer's frame. The resulting spectrum is convolved afterwards to account for the rotational broadening of the lines due to a projected rotation velocity of  $v_{rot} \sin i = 56 \text{ km s}^{-1}$  (Fraser et al. 2010) as denoted in Table 1. This value is lower than earlier measurements from Zuiderwijk (1995) and Howarth et al. (1997) as well as calculations from Falanga et al. (2015), but well motivated by the existence of clearly unblended optical O II lines as demonstrated in Giménez-García et al. (2016). Since this rotational speed is also far from the critical velocity ( $v_{rot} \sin i / v_{rot,crit} \approx 0.15$ ), the convolution method should be sufficient and we thus do not account for rotational effects during our atmosphere calculations.

## 2.2. Hydrodynamic branch

In contrast to standard PoWR models where the mass-loss rate  $\dot{M}$  and the velocity field  $v(r)$  are prescribed in order to essentially measure  $\dot{M}$  and the terminal velocity  $v_\infty$ , hydrodynamically consistent models predict these values by including a depth-dependent solution of the hydrodynamic equation into the main iteration scheme. In a particular hydrodynamic stratification update, the velocity field is obtained by integrating inwards and outwards from the critical point, while the mass-loss rate itself is implicitly fixed by requiring a velocity field that is continuous in  $v(r)$  and  $dv/dr$ .

Despite the fact that  $\dot{M}$  and  $v(r)$  are output quantities, we need to assign them with initial values for the iteration. For this purpose, we use a non-hydrodynamic model that we created based on the results of Giménez-García et al. (2016). Our model also contains additional elements (Ne, Cl, Ar, K, Ca) which were not required for their measurement purposes, but could potentially be important contributors to the radiative acceleration at least in certain depths of the atmosphere.

The approach for obtaining hydrodynamically (HD) consistent PoWR models of the current generation is extensively described in Sander et al. (2017) including an example application to an O4 supergiant ( $\zeta$  Pup/HD 66811). The application to the donor star of Vela X-1 will now demonstrate that the method also works in the much cooler wind regime of an early B-type star.

## 2.3. Inclusion of X-rays

The PoWR models currently can account for the effect of X-rays by assuming a hot and optically thin plasma embedded in

the cool wind. This method, which is described in more detail in Baum et al. (1992), requires three parameters to be specified: the temperature  $T_X$  of the hot component, the fraction with regards to the cool wind component  $X_{fill}$ , and the onset radius  $R_0$ . For  $r > R_0$ , free-free emission and absorption (bremsstrahlung) opacities are considered and the resulting X-rays are covered by the frequency range of the comoving frame radiative transfer. Thereby, the X-rays automatically affect the resulting radiative rates and thus the population numbers, most notably by Auger ionization. In our Vela X-1 models the effect of X-rays is clearly seen, e.g. in the much stronger N V (1238 Å, 1242 Å) doublet compared to a corresponding model not considering X-rays (see Figure 1).

The shortcomings of this approach is that the hot plasma is assumed to be distributed throughout the wind. However, the X-rays resulting from the wind accretion onto a neutron star are generated only locally, thereby breaking the spherical symmetry. Unfortunately, the sophisticated nature of modeling expanding stellar atmospheres so far prevents the detailed use and general application of multi-dimensional approaches. First efforts in this field have been made (see, e.g., Hauschildt & Baron 2006, 2014), but their computational effort is basically overwhelming for a general application, even when using significantly less elements and levels than required for our present task. Thus, performing a detailed radiative transfer is currently limited to 1D model atmospheres, knowing that our consideration of the neutron star effects can only be a rather simple approximation.

In this work, we are using various options to include X-rays. After obtaining an initial HD-consistent stratification for a model without X-rays, we first use the same ad-hoc parameters assumed by Giménez-García et al. (2016), which were motivated chiefly by the aim to reproduce the observed spectrum. Since the X-ray luminosity they needed to assume was much lower than the average observed X-ray luminosity ( $L_X$ ) of Vela X-1, it was interpreted as intrinsic wind X-ray emission (which might stem from e.g. wind shocks). However, the typical X-ray luminosity of OB-stars is nearly two orders of magnitude lower than  $\log L_X/L_{bol} \approx -5.3$  assumed by Giménez-García et al. (2016). The intrinsic wind X-ray emission is best assessed from the observations during the eclipse, for which Schulz et al. (2002) derived  $L_X \approx 2.2 \cdot 10^{33} \text{ erg s}^{-1}$ . We resolved to use this value for potentially intrinsic wind emission albeit this is probably an overestimation, as the radius of the X-ray emitting region centered on the neutron star is likely larger than the donor star's radius.

Finally, we calculated models where in addition to the intrinsic wind X-ray emission we used a second, significantly larger X-ray component that in an approximate way describes the direct X-ray emission from the accreting neutron star. The observed spectrum of the direct component is typically well described as a power law. We approximate the observed X-ray spectrum as a bremsstrahlung, described by a suitable temperature  $T_X$ , and use it in our modeling. The resulting total  $L_X$  corresponds to a typical value for Vela X-1 which is fully sufficient for our study. Giving the caveats in our modeling of the geometry of the X-ray emitting region around the neutron star, our study is rather qualitative and the detailed numbers should be taken with care.

## 3. Results

In non-HD models that are used for empirical studies, usually only those elements and ions need to be considered that either leave an imprint in the spectral appearance, or have a significant influence via blanketing. For hydrodynamically self-consistent

models, however, also all elements and ions which have a non-negligible contribution to the radiative acceleration have to be taken into account. Apart from the additional time required for convergence due to the stratification updates, this is a second factor that makes such kind of models numerically more costly. With a total of 11 elements, the model for Vela X-1 used in Giménez-García et al. (2016) is already quite large. For our purpose in this work, also Ne, Cl, Ar, K, and Ca were added in various ionization stages, raising the total number of considered elements to 16. A detailed list of the considered ions and the number of lines used in the radiative transfer calculations is listed in Table 2. For the model with the larger X-ray component, where we need to account for more of the higher ionization stages, we reduced the number of levels in several of the lower ionization stages. This set of atomic data is listed in parentheses in Table 2. We have cross-checked with test calculations that the smaller number of levels in the lower stages does not notably affect the obtained radiative acceleration as long as the model parameters stay the same.

To get a proper starting model, we calculated a non-HD model with the extended atomic data, but without any X-rays. We obtain a *work ratio*

$$Q := \frac{\dot{M} \int (a_{\text{rad}} - \frac{1}{\rho} \frac{dP}{dr}) dr}{\dot{M} \int (v \frac{dv}{dr} + \frac{GM_*}{r^2}) dr}, \quad (3)$$

which is a measure for the integrated HD balance, of  $Q \approx 1.05$ . As mentioned in the previous section, also the clumping stratification was changed compared to Giménez-García et al. (2016), so we end up with a model slightly differing from the empirical study in some parameters. The full list of input parameters used in all hydrodynamical models presented in this work is given in Table 3. They also differ in various parameters from those used in the study by Krtićka et al. (2012), who derived a mass-loss rate using a comparable approach, but accounting in their METUJE code only for the pure CMF line force (see Krtićka & Kubát 2010). Since they do not provide any emergent spectrum, we prefer the stellar parameters from the empirical results by Giménez-García et al. (2016).

Starting from the previously mentioned non-HD model, the first hydrodynamically consistent model was calculated (first HD model). For this first model, no X-rays were included, so that we simulated the situation for an unperturbed B-star wind with stellar parameters similar to the donor of Vela X-1. This model is not only helpful for comparisons, it is also essential to establish the (electron) temperature stratification  $T_e(r)$  for our follow-up models, since we leave  $T_e(r)$  unchanged when we include X-rays. Already this first model yields a relatively low terminal wind velocity of  $v_\infty = 532 \text{ km s}^{-1}$ , thereby theoretically backing the empirically derived value of  $v_\infty \approx 700 \text{ km s}^{-1}$  determined by Giménez-García et al. (2016). This is also in line with the results from Krtićka et al. (2012), who obtained  $v_\infty = 750 \text{ km s}^{-1}$  in their model without X-rays.

Based on the first HD model, two more HD models were calculated, adopting the previously discussed X-ray parameters corresponding to  $L_X \approx 2.2 \cdot 10^{33} \text{ erg/s}$  and  $L_X \approx 6.7 \cdot 10^{36} \text{ erg/s}$  respectively. Since Giménez-García et al. (2016) used X-ray parameters which correspond to neither of these two cases, we also calculated a model with their X-ray parameters. However, these results turned out to be almost identical to our results using the  $L_X$  motivated by eclipse measurements. Therefore, we refrain from more explicitly discussing this additional X-ray HD model here. Nevertheless it is worth mentioning that the

X-ray implementation in PoWR (see Sect. 2.3) does not necessarily lead to the same value of  $L_X$  if the underlying atomic data are changed. So while Giménez-García et al. (2016) have  $L_X \approx 5 \cdot 10^{33} \text{ erg/s}$ , the HD model with the same  $R_0$ ,  $T_X$  and  $X_{\text{fill}}$  has  $L_X \approx 8 \cdot 10^{34} \text{ erg/s}$ , i.e. the resulting X-ray luminosity is more than an order of magnitude larger due to the direct and indirect effects of the additional elements we added and the slightly different clumping stratification.

It should be noted that even though we use the  $L_X$  measured during eclipse, we do not really describe the accurate geometry of the eclipse situation, since we are working with 1D atmosphere models. We simply choose the  $L_X$  from eclipse as a value for a “moderate” X-ray illumination of the donor wind, meaning that it is way below the unobscured  $L_X$  from the neutron star, but still significantly higher than what one would expect from wind-intrinsic shocks in the donor wind. We therefore also refer to the two cases as “moderate” and “full” illumination test cases in the following. For the moderate case, we use the same X-ray onset radius as Giménez-García et al. (2016), namely  $R_{0,1} \equiv d_0 = 1.2 R_*$ , while in the full case we use the X-rays from the moderate case plus an additional second component with an onset radius  $R_{0,2} = d_{\text{NS}} = 1.8 R_*$ . To avoid multiple indices, we use the terms  $d_0$  and  $d_{\text{NS}}$  in all figures where these onset radii are outlined.

### 3.1. X-ray sensitive UV features

Our first HD model without any X-rays yields  $v_\infty \approx 532 \text{ km s}^{-1}$  together with  $\log \dot{M} = -6.19 [\text{M}_\odot/\text{yr}]$ . As we will show below, our two X-ray test cases will affect the obtained terminal velocity, but leave the mass-loss rate almost unaffected. However, in all cases the X-rays do significantly affect the ionization stratification in the wind and thus can have an imprint on those spectral lines which are originating in the wind, most notably in the UV.

This is demonstrated in Fig. 1 for a selection of UV lines for four different ions, where we compare the averaged observed IUE spectrum with our different hydrodynamically consistent models. The observational data used in this work is identical to Giménez-García et al. (2016), where a more detailed description of the considered observations can be found. While Si III and Si IV are essentially unaffected in the case of moderate X-ray illumination, the absorption trough of the C IV doublet is significantly widened due to an enhanced population of C IV in the wind. For N V the effect is even more spectacular: While it is essentially absent in the outer wind in the model without X-rays, their inclusion offers an ionization source that then substantially populates N V, even when using just the  $L_X$  from the moderate illumination model. The idea that X-rays are responsible for this effect goes back to Cassinelli & Olson (1979) after the discovery of C IV and N V in the *Copernicus* and *Skylab* spectra of stars (Snow & Morton 1976; Parsons et al. 1979) whose winds were too cool to have these ionization stages in radiative equilibrium.

The changes in the ionization stages for our Vela X-1 donor wind model are visualized in Fig. 2, where we compare the relative ground state populations for carbon and nitrogen. One can also see that the leading ionization stage, i.e. the stage most of the ions of an element are populating, is more or less unaffected when considering only the  $L_X$  from the moderate illumination model. This is due to the fact that the population numbers in the leading stage, i.e. C III and N III here, were several orders of magnitude larger than the those of C IV or N V in the model without X-rays and the amount of X-rays in the moderate illumination case is just not high enough to significantly deplete the lower stages. The change in the ionization balance sets in immediately

**Table 2.** Atomic data used in the hydrodynamic models. The numbers in parentheses refer to the model with the high X-ray illumination which requires the inclusion of higher ionization stages.

Ion	Levels	Lines <sup>a</sup>	Ion	Levels	Lines <sup>a</sup>
H I	22	231	Si III	24	69
H II	1	0	Si IV	23 (23)	72 (69)
He I	35	271	Si V	11 (23)	11 (48)
He II	26	325	Si VI	0 (1)	0 (0)
He III	1	0	P III	1 (47)	0 (175)
C I	15 (10)	30 (10)	P IV	12	16
C II	32	148	P V	11	22
C III	40	226	P VI	1	0
C IV	25	230	S I	30 (5)	76 (4)
C V	10	13	S II	32 (15)	80 (18)
C VI	1 (10)	10 (45)	S III	23	38
C VII	0 (1)	0 (0)	S IV	25	54
N I	10	13	S V	10	13
N II	38 (20)	201 (29)	S VI	22 (10)	75 (21)
N III	30	94	S VII	0 (1)	0 (0)
N IV	38	154	Cl III	1	0
N V	20	114	Cl VI	24 (15)	34 (17)
N VI	14	48	Cl V	18	29
N VII	1 (10)	0 (7)	Cl VI	23	46
N VIII	0 (1)	0 (0)	Cl VII	1	0
O I	13 (10)	15 (9)	Ar I	14 (10)	34 (17)
O II	37	150	Ar II	20 (10)	33 (9)
O III	33	121	Ar III	14 (10)	13 (8)
O IV	29	77	Ar IV	13	20
O V	36 (54)	153 (260)	Ar V	10	11
O VI	16	101	Ar VI	9	11
O VII	1 (15)	0 (64)	Ar VII	20	34
O VIII	0 (15)	0 (105)	Ar VIII	1	0
O IX	0 (1)	0 (0)	K I	20 (15)	48 (32)
Ne I	8 (10)	14 (26)	K II	20 (15)	56 (30)
Ne II	18 (10)	40 (9)	K III	20 (10)	40 (12)
Ne III	18	18	K IV	23 (10)	27 (9)
Ne IV	35 (20)	159 (26)	K V	19 (10)	33 (16)
Ne V	20	23	K VI	1	0
Ne VI	20	35	Ca I	20 (15)	35 (24)
Ne VII	1 (10)	0 (11)	Ca II	20 (15)	48 (31)
Ne VIII	0 (10)	0 (20)	Ca III	14	18
Ne IX	0 (10)	0 (13)	Ca IV	24	43
Ne X	0 (10)	0 (13)	Ca V	15	12
Ne XI	0 (1)	0 (0)	Ca VI	15	17
Mg I	1	0	Ca VII	20	28
Mg II	20	57	Ca VIII	1	0
Mg III	20	41	Fe <sup>b</sup> I	1	0
Mg IV	17	27	Fe <sup>b</sup> II	3	2
Al I	10 (1)	16 (0)	Fe <sup>b</sup> III	13	40
Al II	10	11	Fe <sup>b</sup> IV	18	77
Al III	10	18	Fe <sup>b</sup> V	22	107
Al IV	10	10	Fe <sup>b</sup> VI	29	194
Al V	10	9	Fe <sup>b</sup> VII	19	87
Al VI	1	0	Fe <sup>b</sup> VIII	1	0
Si I	20 (3)	45 (2)	Total	1524 (1486)	4976 (4783)
Si II	20	35			

**Notes.** <sup>(a)</sup> Number of transitions with non-negligible oscillator strengths, considered in the radiative transfer calculations <sup>(b)</sup> For Fe, the numbers refer to superlevels and superline transitions which are used to cope with the enormous actual number of lines and transitions. The atom listed as Fe here is actually a generic elements that also includes the further iron group elements Sc, Ti, V, Cr, Mn, Co, and Ni. (See Gräfener et al. 2002, for details.)

**Table 3.** Input parameters for the Vela X-1 donor models

Parameter	Value
$T_*$ [kK]	25.5
$R_*$ [ $R_\odot$ ]	28.4
$\log L$ [ $L_\odot$ ]	5.485
$M_*$ [ $M_\odot$ ]	20.2
$\log g$ [ $\text{cm s}^{-2}$ ]	2.84
$D_\infty$	11
$v_{\text{mic}}$ [ $\text{km s}^{-1}$ ]	10
<i>element</i>	<i>mass fraction</i>
$X_{\text{H}}^a$	0.65
$X_{\text{He}}^a$	0.336
$X_{\text{C}}^a$	$5.0 \times 10^{-4}$
$X_{\text{N}}^a$	$1.8 \times 10^{-3}$
$X_{\text{O}}^a$	$7.0 \times 10^{-3}$
$X_{\text{Ne}}^b$	$1.3 \times 10^{-3}$
$X_{\text{Mg}}^a$	$7.0 \times 10^{-4}$
$X_{\text{Al}}^a$	$7.0 \times 10^{-5}$
$X_{\text{Si}}^a$	$5.5 \times 10^{-4}$
$X_{\text{P}}^a$	$6.4 \times 10^{-6}$
$X_{\text{S}}^a$	$5.0 \times 10^{-4}$
$X_{\text{Cl}}^b$	$8.2 \times 10^{-6}$
$X_{\text{Ar}}^b$	$7.3 \times 10^{-5}$
$X_{\text{K}}^b$	$3.1 \times 10^{-6}$
$X_{\text{Ca}}^b$	$6.1 \times 10^{-5}$
$X_{\text{Fe}}^{a,c}$	$1.4 \times 10^{-3}$

**Notes.** <sup>(a)</sup> Abundance taken from Giménez-García et al. (2016) <sup>(b)</sup> Solar abundance, taken from Asplund et al. (2009) <sup>(c)</sup> Fe includes also the further iron group elements Sc, Ti, V, Cr, Mn, Co, and Ni. See Gräfener et al. (2002) for relative abundances.

where the X-rays are inserted in the moderate illumination case, namely at  $d_0$ .

The whole ionization balance changes significantly for the model applying the full  $L_X$ . Now the lower ionization stages get depleted outwards of  $d_{\text{ns}}$ , where the additional X-ray component is taken into account. The depletion gets even stronger further out at about  $r \gtrsim 2d_{\text{ns}}$  where C v and N vi become the dominant ionization stage. However, the X-ray flux is still not large enough to populate even higher stages such as C vi or N vii. We account for these high ionization stages in our calculations (cf. Table 2) but their population is so low that they are far below the scale in Fig. 2.

Since the full illumination case consists of two X-ray components, setting in at  $d_0$  and  $d_{\text{ns}}$ , we see corresponding changes in the ionization trend at these radii. The third change in the trend at  $r \gtrsim 2d_{\text{ns}}$  does not reflect a change in the X-ray treatment but instead indicates the region where the wind is becoming transparent to X-rays. As the X-rays are more and more depleting the leading opacity sources such as He ii or O iii in outward direction, they are essentially removing the material that would be able to absorb X-rays. Once these lower stages are fully depleted, the wind becomes transparent at X-ray wavelengths and the leading ionization stages change significantly, e.g. to He iii or O vi.

The full X-ray illumination also leaves quite a notable imprint on the UV lines in Fig. 1. The emission parts of C iv and N v lines become stronger and the blue edges of all P Cygni lines shrink, hinting at a lower wind velocity, which is indeed the case as we will see later when discussing the stratification. Since the different amounts of X-ray illumination are a rough approxima-

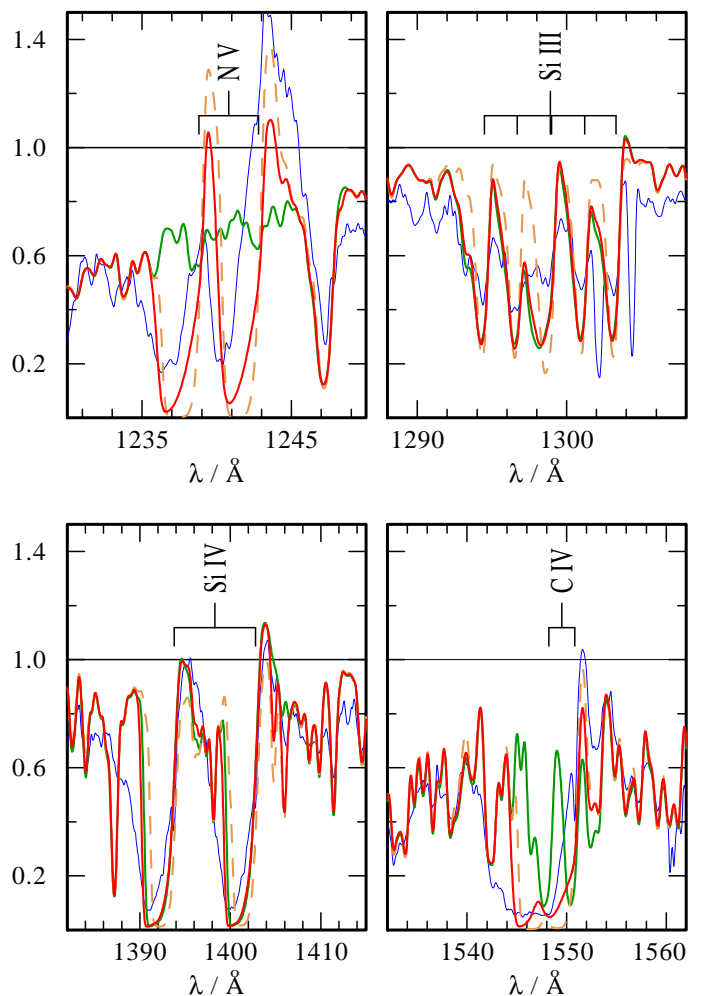


**Fig. 1.** Influence of including X-rays in the atmosphere calculations: The averaged observed spectrum for selected UV lines (blue thin solid line) is compared to HD-PoWR models without (green solid line) as well as with moderate (red solid line) and full X-ray illumination (brown dashed curve).

tion of what we see from a system like Vela X-1 in different orbital phases, our resulting UV line profiles essentially mimic the so-called ‘‘Hatchett-McCray effect’’, i.e. an orbital modulation of the UV lines due to the change in the position of the neutron star and its zone with higher ionization due to the X-rays. This was first discussed by Hatchett & McCray (1977) and has later indeed been found for Vela X-1 by comparing UV spectra from different orbital phases (e.g. Kaper et al. 1993; van Loon et al. 2001). The change of the UV lines of our models agrees also qualitatively with the modeling results from van Loon et al. (2001) who used a radiative transfer code based on the so-called ‘‘Sobolev with exact integration’’ (SEI) method (Lamers et al. 1987).

### 3.2. Mass-loss rates

A compilation of the results from the hydrodynamically-consistent wind models for the donor star of Vela X-1 can be found in Table 4, where we list all three models presented in this work and compare them to the empirical model with prescribed  $v(r)$  by Giménez-García et al. (2016). The mass-loss rates of all three HD models differ by less than 0.1 dex, while the terminal wind velocities vary due to the different X-ray illumination.

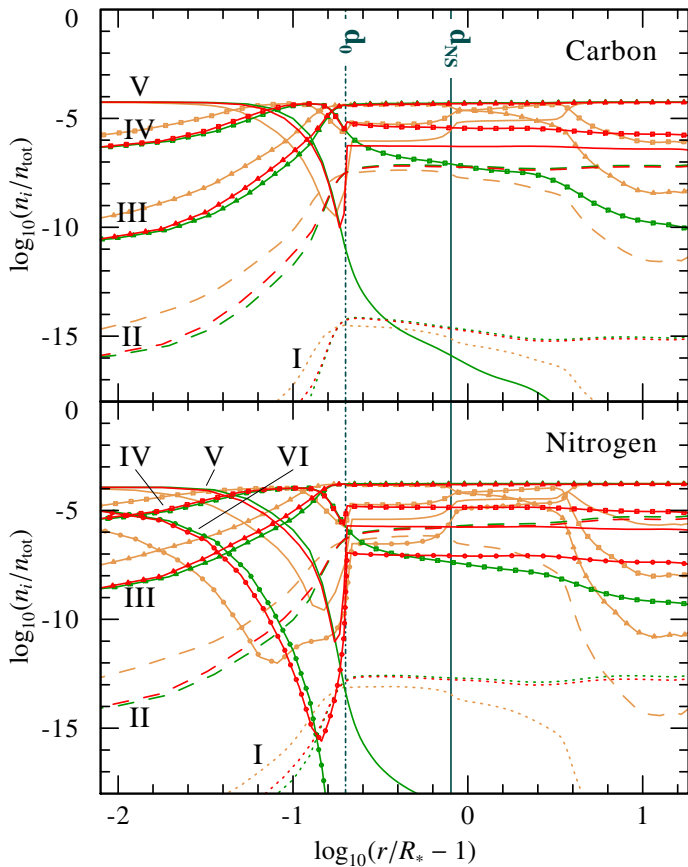


**Fig. 2.** Relative population numbers for the ground state ion levels of carbon (upper panel) and nitrogen (lower panel) in the HD-models with moderate  $L_X$  (red curve), full  $L_X$  (brown dashed curve), and without X-rays (green curve).

While we will discuss the stratification details in the following section, one can already conclude that the X-rays do not largely affect the layers of the critical point and below. The radius of the critical point  $r_c$  essentially stays the same for the moderate X-ray illumination case and moves only slightly inwards for the strong illumination case with the consequence of a tiny increase in the mass-loss rate. The latter is exactly in line with the findings of MacGregor & Vitello (1982) for HMXBs using a simpler, Sobolev-based model and studies that have been performed for intrinsic X-rays in single-star winds (e.g. Krtićka & Kubát 2009).

Our value of the mass-loss rate in the non-X-ray model is  $6.46 \cdot 10^{-7} M_\odot/\text{yr}$ . This is a bit more than a factor of two lower than found by Krtićka et al. (2012), namely  $1.5 \cdot 10^{-6} M_\odot/\text{yr}$ . However, their modeling assumes a smooth wind, while we use a depth-dependent microclumping approach with  $D_\infty = 11$ . A simple comparison by multiplying our  $\dot{M}$  with  $\sqrt{D_\infty} \approx 3.3$  yields  $2.1 \cdot 10^{-6} M_\odot/\text{yr}$ , providing a good agreement, especially considering the fact that Krtićka et al. (2012) use slightly different stellar parameters for the donor star. Since they only account for the pure line force in their models, one would actually expect our  $\dot{M}$  to be a bit higher due to our inclusion of all bound-free and free-free opacities (see also Krtićka & Kubát 2010). Taking a look at the precise slope of our  $D(r)$ , one notices that  $D_\infty$  is not reached at the radius of the critical point  $r_c$  and thus  $\sqrt{D(r_c)} \approx \sqrt{7} \approx 2.65$  might be an even better scaling value for the comparison. Indeed the resulting value of  $1.7 \cdot 10^{-6} M_\odot/\text{yr}$  is even closer to the results from Krtićka et al. (2012), underlining

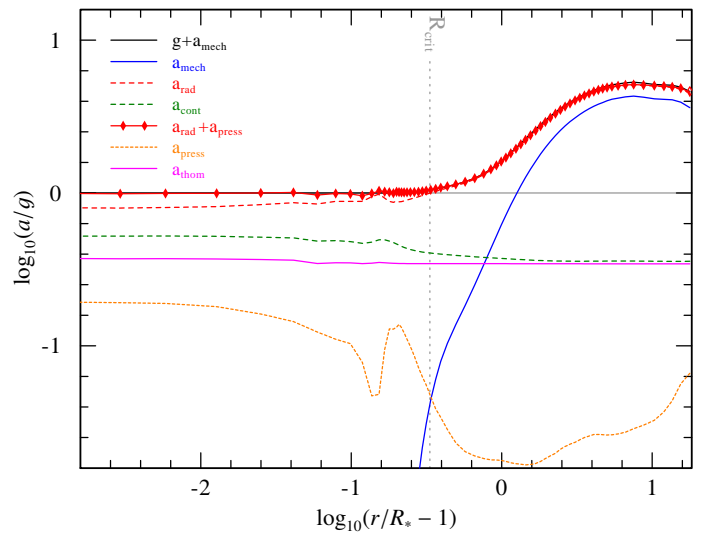


**Fig. 3.** Detailed acceleration stratification for the hydrodynamically consistent model using the moderate X-ray flux. The wind acceleration (thick red diamond line) is compared to the repulsive sum of inertia and gravitational acceleration  $g(r)$  (black line). The input parameters of the model are given in Table 3 while the resulting quantities are listed in Table 4. In order to properly handle the various scales, this is a double-logarithmic plot with all acceleration terms normalized to  $g(r)$ .

that our result for the donor star of Vela X-1 is backed up nicely from both sides, theoretically and empirically.

### 3.3. Stratification

In a HD PoWR model, the outward and inward forces balance each other throughout the whole atmosphere, thus providing a self-consistent stratification. A visual check for the success of the solution method can be done by plotting the different accelerations, namely the total radiative acceleration  $a_{\text{rad}}(r)$ , the acceleration from gas pressure due to temperature and turbulence  $a_{\text{press}}(r)$  as well as the gravitational acceleration  $g(r)$  and the inertia  $a_{\text{mech}}(r) = v(r) \frac{dv}{dr}$ . This is shown in Fig. 3 for the model accounting for moderate X-ray illumination. As one can see, the sum of  $a_{\text{rad}}$  and  $a_{\text{press}}$  matches with the sum of  $g$  and  $a_{\text{mech}}$  throughout the atmosphere and thus our model is indeed hydrodynamically consistent.

Inspection of the contributions from the different accelerations in Fig. 3 reveals that the general picture is very similar to what we obtained for the significantly hotter O supergiant in Sander et al. (2017). In the wind, essentially only the line acceleration and Thomson scattering are important, while in the inner, subsonic regime, also the gas pressure and the contributions from the continuum opacities from bound-free transitions, have to be considered. However, in detail the shapes of the curves differ and the increase of  $a_{\text{rad}}$  beyond the critical point is significantly shallower than in the case of the O supergiant (cf. Fig. 6 in Sander et al. 2017). This is due to the different ions contributing in the temperature regime of an early B-supergiant with  $T_* = 25.5$  kK compared to the 42 kK of the O-star discussed in Sander et al. (2017). The detailed elemental contributions to the driving will be discussed in Sect. 3.5.

A comparison of the velocity field  $v(r)$  from Giménez-García et al. (2016) using a prescribed  $\beta$ -law connected to a consistent hydrostatic solution (see Sander et al. 2015, for technical details) and from our hydrodynamically consistent model is shown in Fig. 4. While we see a sharp increase for  $v(r)$  in the model

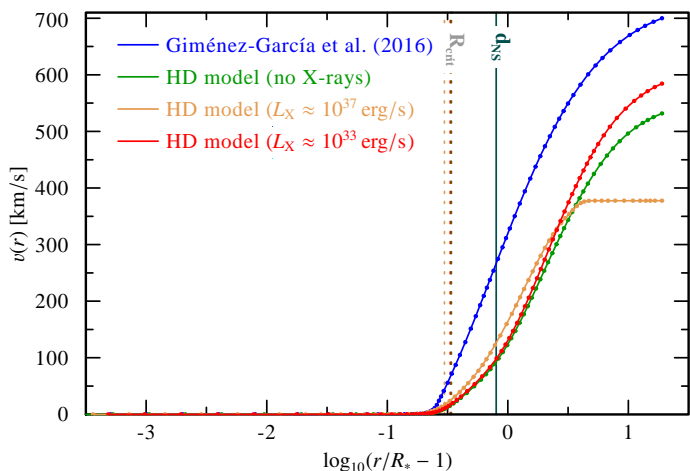


**Fig. 4.** Velocity field for Vela X-1 from Giménez-García et al. (2016) compared to those from the hydrodynamically-consistent models presented in this work using different X-ray fields. The orange line marks the location of the neutron star at a radius of  $d_{\text{ns}} = 1.8 R_*$  from the center of the donor while the colored dashed lines denote the location of the critical point in the corresponding HD models.

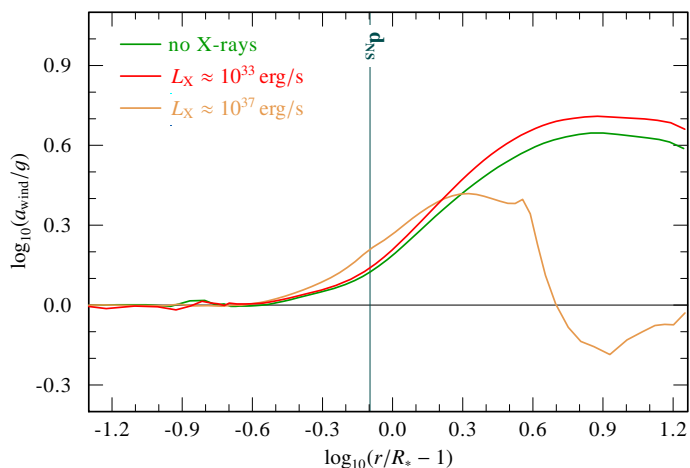


**Fig. 5.** Comparison of the total wind acceleration – normalized to  $g(r)$  – for the three hydrodynamically consistent model using different amounts of X-ray illumination.

from Giménez-García et al. (2016) around and outwards from the sonic point, which marks our critical point in the HD case, the increase is more moderate for the selfconsistent HD-models. A similar situation occurred for the O supergiant model in Sander et al. (2017) and is likely related to two things: First, the  $\beta$ -value used for the prescribed law is – if not simply adopted but motivated by observations – typically inferred from H $\alpha$ . Secondly,  $v(r)$  in the region around the connection point between the quasi-hydrostatic layers and the  $\beta$ -law regime can significantly violate the acceleration balance we are aiming at with our HD models. When using such models to obtain empirical stellar and wind parameters this is usually not a problem, but as soon as one wants to draw conclusions from the detailed stratification, this can lead to errors, most notably in this transition regime.

A closer look reveals that all HD solutions behave rather similar in the inner wind near the critical point, but as we proceed into the outer layers, the effects of the different amount of X-rays become clearly noticeable. In the model with moderate X-ray illumination, the amount of X-rays is just enough to ionize the

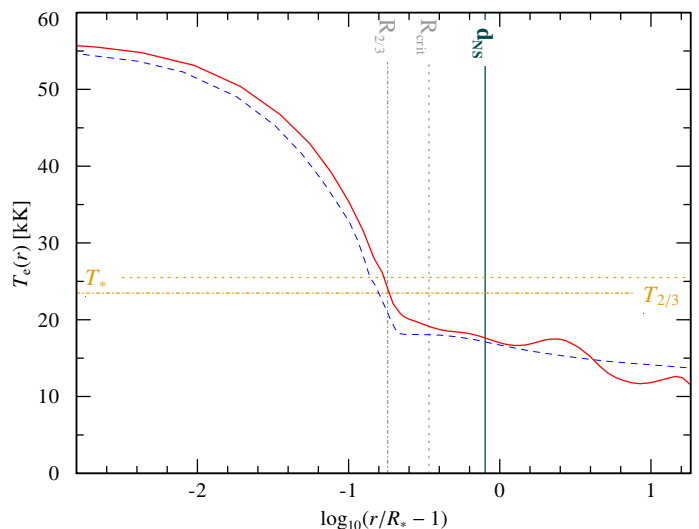


**Fig. 6.** Electron temperature stratification for the hydrodynamically-consistent models (red solid curve) compared to those of a model with a prescribed wind stratification (blue dashed curve) based on Giménez-García et al. (2016). Horizontal lines mark  $T_*$  and  $T_{2/3}$  for the HD-models. Vertical lines denote  $R_{2/3}$  as well as the critical radius for the HD-model without X-rays and the distance of the neutron star.

wind such that the population of some of the driving ions like N v increases and additional driving is provided. However, when the amount of X-rays becomes too high, as we see in the fully X-ray illuminated model, there is so much ionization that important driving ions are depopulated, causing a sharp decrease of the line acceleration in the outer wind. This effect is also illustrated in Fig. 5, where we compare the wind accelerations for all three HD solutions. Here, we further notice that the flattening of the velocity field for the strong illumination case seen in Fig. 4 is actually an artifact due to our technical limitations to monotonic velocity fields in the radiative transfer. Since the normalized wind acceleration drops below unity here, one would have a deceleration in reality and thus an even lower terminal velocity than obtained in this work which we cannot model due to the limitation to monotonic velocity fields. Interestingly, Kaper et al. (1993) already suggested a non-monotonic velocity field for the donor wind of Vela X-1 based on difficulties to model the changes of the UV lines when assuming a monotonic  $v(r)$ , but discussed this with regards to wind-intrinsic instabilities and not wind deceleration due to X-ray ionization.

Although the radiative acceleration drops for  $r \gtrsim 2d_{\text{ns}}$ , Fig. 5 also illustrates that it does not vanish completely and the wind might therefore not be shut off completely, even in the strongly ionized region. Our quite approximate X-ray treatment might be a caveat here, but it is noteworthy that the large breakdown of the acceleration and thus the strongest effect of the X-rays does not occur at the distance of the neutron star, but instead much further outside for  $r \gtrsim 3 R_* \approx 2d_{\text{ns}}$  where the stratification becomes optically thin also for X-ray wavelengths and the ionization balance changes as discussed in Sect. 3.1. A more sophisticated treatment of the situation would be needed to verify these results, but this could potentially have interesting consequences for the proper wind treatment in multi-dimensional, time-dependent hydrodynamical simulations of HMXBs.

The (electron) temperature stratification  $T_e(r)$  for all HD models is displayed in Fig. 6, where we also show the stratification from Giménez-García et al. (2016) for comparison. The results do not differ much, but the HD model turns out to be



**Table 4.** Results from the hydrodynamically consistent model for the Vela X-1 donor star HD 77581

Quantity	GG2016 <sup>a</sup>		HD models	
	empirical	no $L_X$	“moderate” <sup>b</sup>	“full” <sup>c</sup>
$\log L_X$ [erg s <sup>-1</sup> ]	33.7	–	33.4	36.9
$R_{\text{crit}} [R_*$ ]	–	1.34	1.33	1.30
$\log \dot{M} [M_\odot \text{ yr}^{-1}]$	-6.20	-6.19	-6.18	-6.07
$v_\infty$ [km s <sup>-1</sup> ]	700	532	584	378
$\log R_t [R_\odot]$	2.20	2.12	2.14	1.94
$\log Q_{\text{ws}}$ [cgs]	-12.12	-11.94	-11.99	-11.60
$T_{2/3}$ [kK]	24.4	23.5	23.5	23.8
$q_{\text{ion}}$	0.77	0.75	0.75	0.77
$\Gamma_e$	0.34	0.35	0.35	0.36
$\eta = \dot{M} v_\infty c / L$	0.07	0.06	0.06	0.05
$\log D_{\text{mom}}^d$	28.7	28.6	28.6	28.6

**Notes.** <sup>(a)</sup> Empirical values derived by Giménez-García et al. (2016) <sup>(b)</sup> moderate X-ray illumination of the donor wind with  $L_X$  corresponding to eclipse measurement <sup>(c)</sup> full X-ray illumination of the donor wind with  $L_X$  corresponding to an unobscured NS situation <sup>(d)</sup> Modified wind momentum in units of  $\text{g cm s}^{-2} R_\odot^{-1/2}$ , defined as  $D_{\text{mom}} = \dot{M} v_\infty \sqrt{R_*/R_\odot}$  (see, e.g., Kudritzki & Puls 2000)

slightly hotter in the inner part and has minor non-monotonic parts in the outer wind. Furthermore, the region between  $R_{\text{crit}}$  and  $R_{2/3}$  is more smooth, which likely results from the fact that the HD-stratification avoids artifacts which can arise when connecting the velocity fields of the subsonic and the wind regime.

The stratifications from all three hydrodynamically consistent wind models are provided as tables in the appendix A.

### 3.4. Accretion estimation

In the so-called “wind-fed HMXBs”, the wind of the donor star is accreted by the compact object, in our case a neutron star. The empirical results from Giménez-García et al. (2016) place Vela X-1 in the so-called “direct accretion regime”, using the scheme from Bozzo et al. (2008). Since our results for the mass-loss rate essentially confirm their findings and the wind velocity at the distance of the neutron star is even a bit lower than the one inferred from the prescribed law by Giménez-García et al. (2016), the assumption that Vela X-1 is set in the “direct accretion regime” is corroborated by our results. For this case, we can expect the X-ray luminosity  $L_X$  to be roughly of the order of the accretion luminosity  $L_{\text{acc}}$ , which we estimate via Bondi-Hoyle-Lyttleton (BHL) accretion (Hoyle & Lyttleton 1939; Bondi & Hoyle 1944; Davidson & Ostriker 1973). A more detailed discussion about BHL accretion and the different accretion regimes can be found in the recent review by Martínez-Núñez et al. (2017).

The Bondi-Hoyle radius or “accretion radius”

$$R_{\text{acc}} = \frac{2GM_{\text{NS}}}{v_{\text{rel}}^2} \quad (4)$$

describes the radius around the neutron star within wind material can be captured and accreted.  $M_{\text{NS}}$  denotes the mass of the neutron star and  $G$  is the gravitational constant. The relevant velocity for  $R_{\text{acc}}$  is the relative velocity  $v_{\text{rel}}$  between the neutron star and the donor wind, resulting from the radial wind velocity  $v(r = d_{\text{NS}})$  and the orbital velocity of the neutron star,  $v_{\text{orb}}$ .

For a circular orbit, which is quite a good approximation for the case of Vela X-1 ( $e \lesssim 0.1$ , see Table 1), the vector calculation simplifies to

$$v_{\text{rel}} = \sqrt{v_{\text{orb}}^2 + v^2(d_{\text{NS}})}. \quad (5)$$

When estimating the relative velocity, a common assumption is to use  $v_{\text{rel}} \approx v(d_{\text{NS}})$  assuming that the orbital velocity is much smaller than the wind velocity ( $v_{\text{orb}}^2 \ll v^2(d_{\text{NS}})$ ). Since the shape of the velocity field is usually unknown, assuming  $v(d_{\text{NS}}) \approx v_\infty$  is sometimes assumed as well, which would allow us to replace  $v_{\text{rel}}$  with  $v_\infty$  in Eq. (4). However, both assumptions cannot be taken for granted for a particular system and thus can lead to significant errors in the accretion estimation if used inadvertently. Typical orbital separations are  $d_{\text{NS}} \approx 2R_*$  at which it is by no means guaranteed that the wind has already reached its terminal velocity.

In the case of Vela X-1, the neutron star seems to be located even a bit closer. Using the velocity field from our model with moderate X-ray illumination, we predict a value of  $v(d_{\text{NS}})$  that is almost an order of magnitude lower than  $v_\infty$ , i.e. this would be causing a huge error due the steep velocity dependence as we will see in the further calculation. For other systems this error might be smaller, but overestimating  $v_{\text{rel}}$  by a factor of 2 would be actually rather typical when assuming  $v(d_{\text{NS}}) \approx v_\infty$ . Secondly, the low wind velocity at the distance of the neutron star also means that the assumption  $v_{\text{orb}}^2 \ll v^2(d_{\text{NS}})$  is not true. Already with the prescribed velocity field, Giménez-García et al. (2016) had  $v_{\text{orb}} \approx v(d_{\text{NS}})$ . The hydrodynamically-consistent solution now predicts that the wind velocity at the location of the neutron star is even lower than the orbital speed of the compact object. Thus Eq. (5) yields in our case  $v_{\text{rel}} \approx 300 \text{ km s}^{-1}$ .

Assuming that the potential energy from the accreted matter is completely converted into X-rays, one obtains the accretion luminosity,

$$L_{\text{acc}} = \frac{GM_{\text{NS}}\dot{M}_{\text{acc}}}{R_{\text{NS}}} \quad (6)$$

with  $R_{\text{NS}}$  denoting the radius of the neutron star and  $\dot{M}_{\text{acc}}$  the mass accretion rate. Assuming direct wind accretion, the latter can be expressed as

$$\dot{M}_{\text{acc}} = \zeta \pi R_{\text{acc}}^2 v_{\text{rel}} \rho(d_{\text{NS}}) \quad (7)$$

where  $\zeta$  is a numerical factor introduced to correct for radiation pressure and finite gas cooling. For moderately luminous X-ray sources this is usually taken as  $\zeta \equiv 1$ . Approximating the density  $\rho(d_{\text{NS}})$  with the one from a stationary, spherically symmetric wind, we can write

$$\rho(d_{\text{NS}}) = \frac{\dot{M}_{\text{donor}}}{4\pi d_{\text{NS}}^2 v(d_{\text{NS}})}. \quad (8)$$

This allows us to rewrite Eq. (7) such that we can express the accretion rate with the wind mass-loss rate of the donor star, i.e.

$$\dot{M}_{\text{acc}} = \zeta \frac{R_{\text{acc}}^2}{4d_{\text{NS}}^2} \frac{v_{\text{rel}}}{v(d_{\text{NS}})} \dot{M}_{\text{donor}}. \quad (9)$$

Now plugging Eq. (9) into Eq. (6) and replacing  $R_{\text{acc}}$  with the help of Eq. (4), we obtain

$$L_{\text{acc}} = \frac{GM_{\text{NS}}}{R_{\text{NS}}} \dot{M}_{\text{acc}} \quad (10)$$

$$= \zeta \frac{GM_{\text{NS}}}{R_{\text{NS}}} \frac{R_{\text{acc}}^2}{4d_{\text{NS}}^2} \frac{v_{\text{rel}}}{v(d_{\text{NS}})} \dot{M}_{\text{donor}} \quad (11)$$

$$= \zeta \frac{(GM_{\text{NS}})^3}{R_{\text{NS}}} \frac{\dot{M}_{\text{donor}}}{d_{\text{NS}}^2 v_{\text{rel}}^3 v(d_{\text{NS}})} \quad (12)$$

which eventually allows us to estimate  $L_{\text{acc}}$  using our results. Applying typical values for the neutron star ( $M_{\text{NS}} = 1.4 M_{\odot}$ ,  $R_{\text{NS}} = 12 \text{ km}$ ,  $d_{\text{NS}} = 1.8 R_*$ ,  $v_{\text{NS}} = 281 \text{ km s}^{-1}$ ) and inferring a value of  $v(d_{\text{NS}}) \approx 100 \text{ km s}^{-1}$  from our HD model, which we essentially find regardless of the particular X-ray illumination, we find

$$L_{\text{acc}} \approx \zeta \cdot 6.5 \dots 8.7 \cdot 10^{37} \text{ erg/s.} \quad (13)$$

This is on the order of what we used as  $L_X$  in our strong illumination test case. Due to the lower value of  $v(d_{\text{NS}})$  compared to Giménez-García et al. (2016), our value of  $L_{\text{acc}}$  is almost an order of magnitude higher, resulting from the fact that  $L_{\text{acc}}$  roughly scales with the inverse of this quantity to the fourth power. Although the average X-ray luminosity  $\langle L_X \rangle \approx 4.5 \cdot 10^{36} \text{ erg/s}$  (Sako et al. 1999; Fürst et al. 2010) is also an order of magnitude lower, our estimate is still remarkably consistent given that we assume accretion to be so efficient that all energy is converted into X-ray luminosity. Since the BHL estimate is likely an upper limit, as hinted by simulations performed for accretion in binaries (e.g. Theuns et al. 1996), it is not uncommon to introduce an accretion efficiency parameter  $\eta_{\text{eff}}^{\text{acc}} = L_X/L_{\text{acc}}$  – sometimes also termed transformation factor – which is typically assumed to be around  $\eta_{\text{eff}}^{\text{acc}} \approx 0.1 \dots 0.3$  (e.g. Negueruela 2010; Oskinova et al. 2012). In our case, a value of 0.1 would lead to an excellent agreement between our estimate and the observed  $\langle L_X \rangle$ .

### 3.5. Wind driving

We can get a more detailed look into the wind driving by studying the contributions of the various elements to the radiative acceleration, as illustrated in Fig. 7 for the model using the moderate X-ray flux. At solar metallicity, the iron opacities are the main line contributions to the driving until the sonic point and further outwards up to about  $2 R_*$ . While this appears to be rather similar to the much hotter O-supergiant ( $\zeta$  Pup) model from Sander et al. (2017), it is noteworthy that the iron contribution already outweighs the free electron (Thomson) scattering contribution at the sonic point in the case of Vela X-1. This is not the case for  $\zeta$  Pup, where the main ion contributing to the iron acceleration fraction is Fe v instead of Fe III here, which can be seen in Fig. 8 where the relative contributions of the various ions in the wind are shown. The different temperature and thus ionization regime also leads to the effect that we see some differences in the list of elements providing major contributions in the outer wind: After a few  $R_*$ , sulfur, nitrogen, and the iron group (in descending order) all provide between 15% and 20% of the radiative force. Slightly smaller contributions stem from Si and C. Oxygen provides about 5% which is already below the Thomson contribution. Interestingly, it is followed by hydrogen – due to its significant continuum contribution – and then several elements (Al, Cl, P, Ar) contributing on a percentage level. The driving influence of K is already two orders of magnitude lower than that of the leading elements and below the basically negligible gas pressure. The remaining elements (He, Ne, Mg, Ca) have even lower contributions and thus can be neglected with regards to driving. However, as the comparison with the  $\zeta$  Pup model from Sander et al. (2017) illustrates, one has to be cautious when generalizing these results. The influence of the various elements depends strongly on the abundances and the ionization stages and thus the picture can change drastically when transitioning to other temperature and/or abundance regimes. We are planning to investigate this in more detail in future studies.

## 4. Conclusions

We constructed hydrodynamically consistent PoWR models for the donor star of Vela X-1, HD 77581, thereby for the first time applying our recently introduced next-generation PoWR models (Sander et al. 2017) to the regime of early B-supergiants. The stellar parameters are motivated by the previous empirical study from Giménez-García et al. (2016), and the resulting models reproduce the overall spectral appearance of the donor star. Three hydrodynamically consistent models using different levels of X-ray illuminations demonstrate the effects of the X-rays arising from accretion onto the neutron star in the Vela X-1 system on the donor star wind.

Our atmosphere models prove that the low terminal velocity derived by Giménez-García et al. (2016) is consistent with the radiative acceleration provided by the radiation of the donor star, in line with earlier predictions by Krtićka et al. (2012). In the inner wind region, our hydrodynamical models yield a stratification that is notably different from what one obtains when using a prescribed  $\beta$ -law. Our calculations furthermore reveal that a certain amount of X-rays influences the ionization balance such that additional driving is provided in the outer wind, and the terminal velocity is increased by about 10% compared to a similar donor star without X-rays. However, when the X-ray illumination is too high, a breakdown of the acceleration occurs in the outer wind. It is noteworthy that this breakdown does not occur already at the distance of the neutron star  $d_{\text{NS}}$ , but instead much further out after  $r \gtrsim 3 R_* \approx 2 d_{\text{NS}}$ . Nevertheless, due to the restriction to a stationary 1D description of the wind and a rather approximate X-ray treatment this result should be taken with care.

Our calculations confirm the empirically derived mass-loss rate of the donor star of Vela X-1 of  $\log \dot{M} \approx -6.2 [M_{\odot}/\text{yr}]$  assuming a depth-dependent microclumping with  $D_{\infty} = 11$ . The X-ray illumination has only very little influence on the wind mass loss, potentially increasing the rate by up to 0.1 dex in the direction towards the neutron star. The wind velocity in the inner wind and especially at the distance of the neutron star  $v(d_{\text{NS}}) \approx 100 \text{ km s}^{-1}$  is lower than typically estimated from prescribed  $\beta$ -laws. Our obtained  $v(d_{\text{NS}})$  is lower than the orbital speed of the neutron star, but an estimate assuming direct Bondi-Hoyle-Littleton accretion yields excellent agreement between the mean observed X-ray luminosity of Vela X-1 and our prediction. Tables with the stratifications from all the hydrodynamically consistent models are provided in appendix A as well as in an electronic form.

A detailed inspection of the driving contributions reveals that a plethora of ions from more than 10 different elements need to be considered for properly reconstructing the full radiative wind acceleration. The leading ion in our early B-type supergiant wind is Fe III which contributes about 15% in the case of a moderate X-ray illumination. In the outer wind, S III reaches an almost comparable fraction, followed by Si III and C III contributing about 10% in the wind. Although the general picture of the B-supergiant wind shows similarities to our previous O-supergiant results (Sander et al. 2017), the detailed contributions are significantly different due to the different stellar parameters. Further studies are required before more general conclusions should be drawn.

*Acknowledgements.* A.A.C. Sander is supported by the Deutsche Forschungsgemeinschaft (DFG) under grant HA 1455/26. T.S. acknowledges support from the German “Verbundforschung” (DLR) grant 50 OR 1612. This research made use of the SIMBAD and VizieR databases, operated at CDS, Strasbourg, France. This publication was motivated by a team meeting sponsored by the International Space Science Institute at Bern, Switzerland. We acknowledge support from the Faculty of the European Space Astronomy Centre (ESAC).

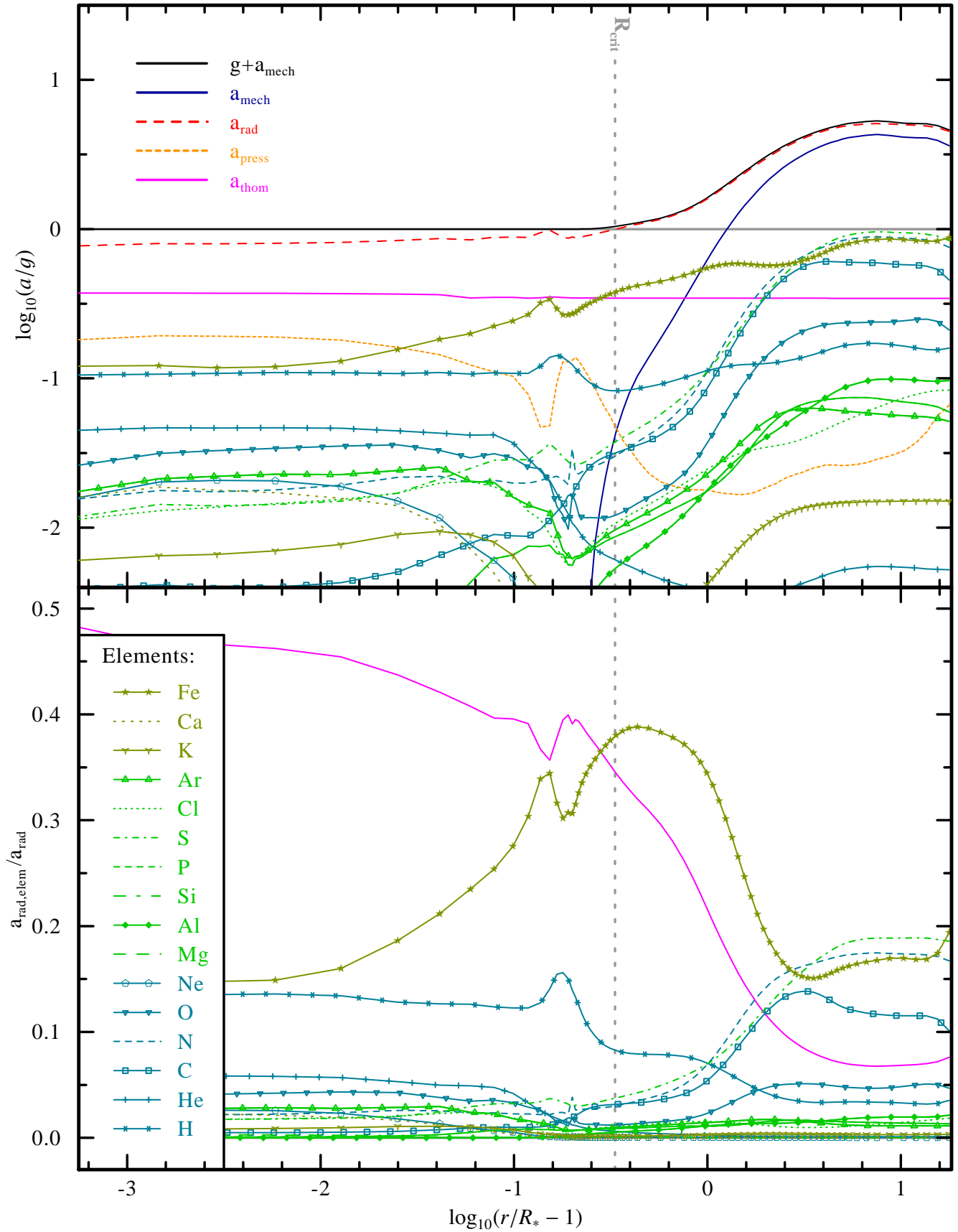


**Fig. 7.** Absolute (upper panel) and relative (lower panel) contributions to the radiative acceleration from the different elements considered in the hydrodynamically-consistent atmosphere model incorporating the moderate X-ray flux. The total radiative acceleration and the acceleration due to gas pressure are also shown in the upper panel for comparison. The lower panel shows the fraction that electron scattering (pink solid curve) and the various elements contribute to the total radiative acceleration.

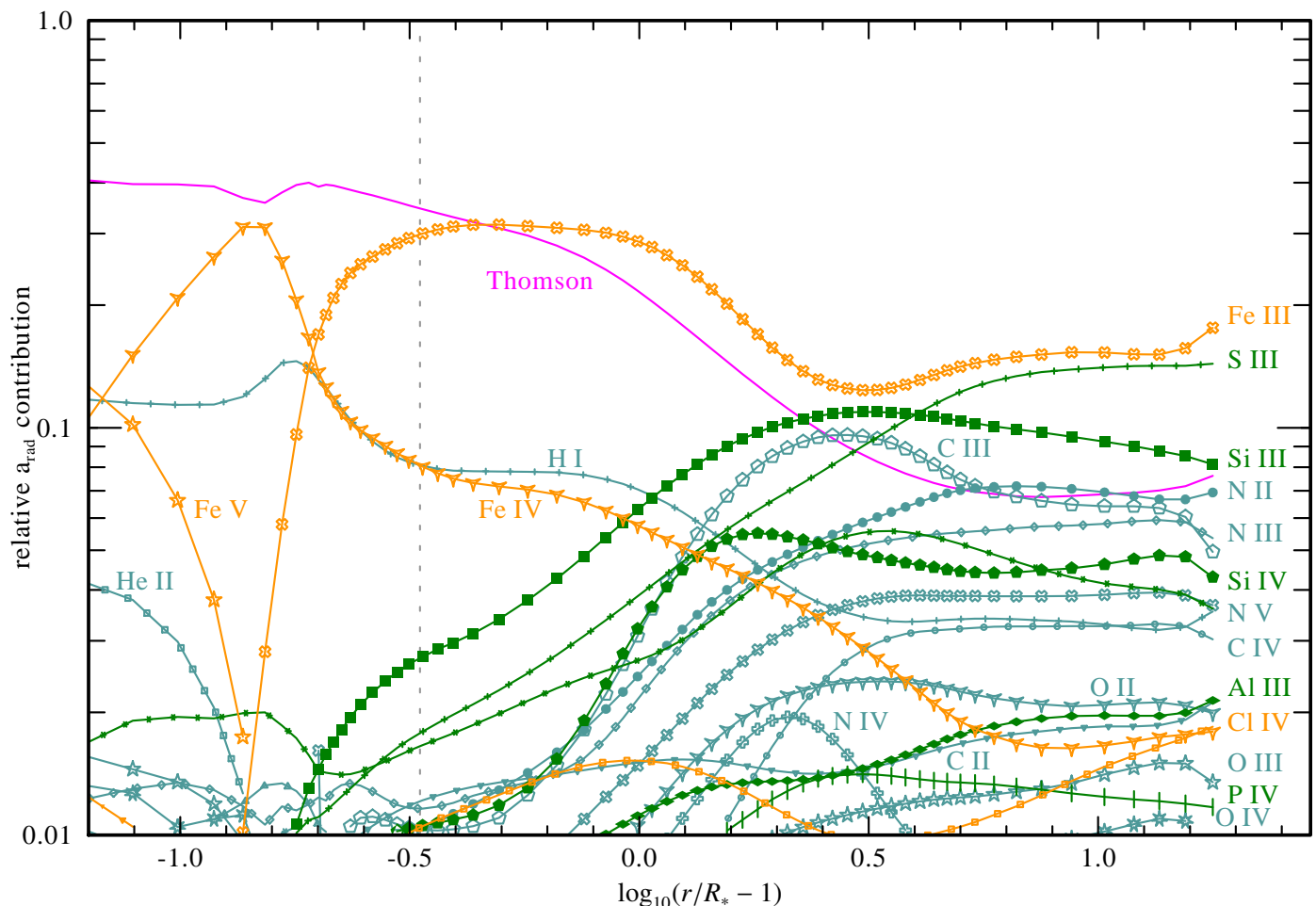


**Fig. 8.** Relative contributions to the radiative acceleration from the different ions (colored curves with various symbols) and due to scattering by free electrons (pink solid curve). Only ions which contribute at least 1% to the radiative acceleration are shown. For a better visibility of the various contributions on a percentage level, the y-axis is shown on a logarithmic scale.

## References

- Asplund, M., Grevesse, N., Sauval, A. J., & Scott, P. 2009, *ARA&A*, 47, 481
- Baum, E., Hamann, W.-R., Koesterke, L., & Wessolowski, U. 1992, *A&A*, 266, 402
- Bildsten, L., Chakrabarty, D., Chiu, J., et al. 1997, *ApJS*, 113, 367
- Blondin, J. M., Kallman, T. R., Fryxell, B. A., & Taam, R. E. 1990, *ApJ*, 356, 591
- Blondin, J. M. & Pope, T. C. 2009, *ApJ*, 700, 95
- Blondin, J. M., Stevens, I. R., & Kallman, T. R. 1991, *ApJ*, 371, 684
- Bondi, H. & Hoyle, F. 1944, *MNRAS*, 104, 273
- Bozzo, E., Falanga, M., & Stella, L. 2008, *ApJ*, 683, 1031
- Cassinelli, J. P. & Olson, G. L. 1979, *ApJ*, 229, 304
- Castor, J. I., Abbott, D. C., & Klein, R. I. 1975, *ApJ*, 195, 157
- Chodil, G., Mark, H., Rodrigues, R., Seward, F. D., & Swift, C. D. 1967, *ApJ*, 150, 57
- Davidson, K. & Ostriker, J. P. 1973, *ApJ*, 179, 585
- Falanga, M., Bozzo, E., Lutovinov, A., et al. 2015, *A&A*, 577, A130
- Fraser, M., Dufton, P. L., Hunter, I., & Ryans, R. S. I. 2010, *MNRAS*, 404, 1306
- Fürst, F., Kreykenbohm, I., Pottschmidt, K., et al. 2010, *A&A*, 519, A37
- Giménez-García, A., Shenar, T., Torrejón, J. M., et al. 2016, *A&A*, 591, A26
- Gräfener, G., Koesterke, L., & Hamann, W.-R. 2002, *A&A*, 387, 244
- Hamann, W.-R. & Gräfener, G. 2003, *A&A*, 410, 993
- Hatchett, S. & McCray, R. 1977, *ApJ*, 211, 552
- Hauschildt, P. H. & Baron, E. 2006, *A&A*, 451, 273
- Hauschildt, P. H. & Baron, E. 2014, *A&A*, 566, A89
- Howarth, I. D., Siebert, K. W., Hussain, G. A. J., & Prinja, R. K. 1997, *MNRAS*, 284, 265
- Hoyle, F. & Lyttleton, R. A. 1939, *Proceedings of the Cambridge Philosophical Society*, 35, 405
- Kaper, L., Hammerschlag-Hensberge, G., & van Loon, J. T. 1993, *A&A*, 279, 485
- Kreykenbohm, I., Wilms, J., Kretschmar, P., et al. 2008, *A&A*, 492, 511
- Krtićka, J. & Kubát, J. 2009, *MNRAS*, 394, 2065
- Krtićka, J. & Kubát, J. 2010, *A&A*, 519, A50
- Krtićka, J., Kubát, J., & Krtićková, I. 2015, *A&A*, 579, A111
- Krtićka, J., Kubát, J., & Skalický, J. 2012, *ApJ*, 757, 162
- Kudritzki, R.-P. & Puls, J. 2000, *ARA&A*, 38, 613
- Lamers, H. J. G. L. M., Cerruti-Sola, M., & Perinotto, M. 1987, *ApJ*, 314, 726
- MacGregor, K. B. & Vitello, P. A. J. 1982, *ApJ*, 259, 267
- Manousakis, A. & Walter, R. 2015, *A&A*, 584, A25
- Martínez-Núñez, S., Kretschmar, P., Bozzo, E., et al. 2017, *Space Sci. Rev.*
- Martínez-Núñez, S., Torrejón, J. M., Kühnel, M., et al. 2014, *A&A*, 563, A70
- Nagase, F., Zylstra, G., Sonobe, T., et al. 1994, *ApJ*, 436, L1
- Negueruela, I. 2010, in *Astronomical Society of the Pacific Conference Series*, Vol. 422, *High Energy Phenomena in Massive Stars*, ed. J. Martí, P. L. Luque-Escamilla, & J. A. Combi, 57
- Oskinova, L. M., Feldmeier, A., & Kretschmar, P. 2012, *MNRAS*, 421, 2820
- Parsons, S. B., Wray, J. D., Henize, K. G., & Benedict, G. F. 1979, in *IAU Symposium*, Vol. 83, *Mass Loss and Evolution of O-Type Stars*, ed. P. S. Conti & C. W. H. De Loore, 95–98
- Sako, M., Liedahl, D. A., Kahn, S. M., & Paerels, F. 1999, *ApJ*, 525, 921
- Sander, A., Shenar, T., Hainich, R., et al. 2015, *A&A*, 577, A13
- Sander, A. A. C., Hamann, W.-R., Todt, H., Hainich, R., & Shenar, T. 2017, *ArXiv e-prints*
- Sato, N., Hayakawa, S., Nagase, F., et al. 1986, *PASJ*, 38, 731
- Schulz, N. S., Canizares, C. R., Lee, J. C., & Sako, M. 2002, *ApJ*, 564, L21
- Snow, Jr., T. P. & Morton, D. C. 1976, *ApJS*, 32, 429
- Theuns, T., Boffin, H. M. J., & Jorissen, A. 1996, *MNRAS*, 280, 1264
- van Kerkwijk, M. H., van Paradijs, J., Zuiderwijk, E. J., et al. 1995, *A&A*, 303, 483
- van Loon, J. T., Kaper, L., & Hammerschlag-Hensberge, G. 2001, *A&A*, 375, 498
- Zuiderwijk, E. J. 1995, *A&A*, 299, 79

**Appendix A: Stratifications of our hydrodynamically consistent wind models for the donor star of Vela X-1****Table A.1.** Stratification for the atmosphere model without any X-ray illumination

$r - R_*$ [ $R_*$ ]	$v$ [ $\text{km s}^{-1}$ ]	$T_e$ [kK]	$\log n_{\text{tot}}$ [ $\text{cm}^{-3}$ ]	$\log n_e$ [ $\text{cm}^{-3}$ ]
19.0	531.7	11.209	7.239	7.240
16.2	525.3	12.449	7.378	7.378
14.5	520.2	12.620	7.471	7.472
13.1	514.9	12.421	7.555	7.555
11.6	507.3	12.116	7.662	7.662
9.92	496.2	11.790	7.795	7.795
8.46	482.7	11.666	7.932	7.932
7.44	469.9	11.798	8.042	8.043
6.64	457.3	12.052	8.141	8.141
5.88	442.3	12.447	8.246	8.246
5.18	424.9	13.074	8.357	8.358
4.61	407.7	13.917	8.459	8.459
4.23	393.9	14.654	8.535	8.536
3.93	381.9	15.268	8.600	8.600
3.66	369.9	15.734	8.661	8.662
3.41	357.4	16.244	8.724	8.725
3.16	343.5	16.643	8.792	8.793
2.93	329.0	16.992	8.862	8.862
2.72	315.0	17.268	8.927	8.928
2.53	300.6	17.439	8.994	8.994
2.34	284.9	17.506	9.066	9.066
2.16	268.8	17.466	9.139	9.139
2.00	253.7	17.371	9.208	9.208
1.86	238.6	17.221	9.277	9.278
1.71	222.3	17.025	9.353	9.353
1.58	206.1	16.832	9.430	9.430
1.47	191.3	16.703	9.502	9.502
1.36	176.9	16.653	9.574	9.575
1.25	161.8	16.658	9.653	9.653
1.15	147.3	16.716	9.733	9.733
1.07	134.4	16.843	9.808	9.808
0.988	122.3	17.033	9.883	9.883
0.909	110.1	17.258	9.964	9.964
0.836	98.62	17.490	10.045	10.046
0.774	88.84	17.718	10.121	10.121
0.716	79.90	17.926	10.195	10.196
0.659	70.97	18.111	10.276	10.277
0.597	61.17	18.269	10.374	10.374
0.525	49.51	18.400	10.506	10.506
0.456	37.76	18.527	10.664	10.664
0.407	29.12	18.686	10.806	10.807
0.378	23.71	18.848	10.914	10.914
0.353	19.18	19.022	11.022	11.022
0.330	15.00	19.217	11.143	11.144
0.313	12.03	19.390	11.251	11.251
0.298	9.653	19.553	11.356	11.356
0.282	7.249	19.736	11.491	11.492
0.266	5.236	19.912	11.643	11.644
0.253	3.842	20.059	11.787	11.787
0.242	2.869	20.207	11.921	11.921
0.233	2.172	20.397	12.049	12.049
0.225	1.662	20.631	12.170	12.171
0.217	1.282	20.940	12.289	12.289
0.209	0.9318	21.409	12.433	12.434
0.197	0.5911	22.090	12.639	12.640
0.183	0.3463	23.810	12.882	12.882
0.167	0.2219	26.160	13.087	13.088

**Table A.1.** continued.

$r - R_*$ [ $R_*$ ]	$v$ [ $\text{km s}^{-1}$ ]	$T_e$ [kK]	$\log n_{\text{tot}}$ [ $\text{cm}^{-3}$ ]	$\log n_e$ [ $\text{cm}^{-3}$ ]
0.147	0.1680	27.980	13.222	13.228
0.125	0.1492	31.635	13.291	13.310
0.100	0.1173	35.394	13.415	13.449
0.767E-01	0.8363E-01	39.214	13.581	13.624
0.551E-01	0.5715E-01	42.973	13.764	13.810
0.354E-01	0.3785E-01	46.686	13.959	14.007
0.194E-01	0.2584E-01	50.354	14.138	14.186
0.954E-02	0.2002E-01	53.118	14.257	14.305
0.424E-02	0.1743E-01	54.807	14.322	14.370
0.212E-02	0.1649E-01	55.523	14.348	14.396
0.106E-02	0.1599E-01	55.913	14.362	14.411
0.531E-03	0.1571E-01	55.970	14.370	14.419
0.00	0.1562E-01	56.148	14.373	14.422

**Table A.3.** Stratification for the atmosphere model with moderate X-ray illumination ( $L_X \approx 10^{33}$  erg/s)

$r - R_*$ [ $R_*$ ]	$v$ [ $\text{km s}^{-1}$ ]	$T_e$ [kK]	$\log n_{\text{tot}}$ [ $\text{cm}^{-3}$ ]	$\log n_e$ [ $\text{cm}^{-3}$ ]
19.0	584.5	11.209	7.212	7.212
16.5	578.3	12.192	7.330	7.331
14.4	571.1	12.576	7.447	7.448
12.8	563.4	12.402	7.553	7.553
11.2	553.9	12.107	7.667	7.667
9.48	540.2	11.803	7.807	7.808
8.03	523.7	11.704	7.950	7.951
7.02	508.3	11.835	8.066	8.066
6.25	493.0	12.086	8.168	8.168
5.61	477.7	12.429	8.261	8.261
5.18	465.2	12.775	8.331	8.332
4.84	454.2	13.147	8.391	8.391
4.53	442.9	13.594	8.449	8.449
4.24	430.9	14.112	8.508	8.509
3.94	417.5	14.707	8.572	8.573
3.67	403.3	15.275	8.637	8.638
3.42	389.3	15.786	8.700	8.701
3.18	374.7	16.242	8.764	8.764
2.95	358.5	16.652	8.833	8.833
2.73	341.7	17.003	8.903	8.904
2.54	325.6	17.264	8.970	8.970
2.36	309.2	17.439	9.037	9.037
2.19	291.5	17.485	9.110	9.110
2.02	273.5	17.452	9.184	9.184
1.88	256.9	17.357	9.253	9.253
1.75	240.6	17.208	9.322	9.323
1.61	223.2	17.020	9.397	9.398
1.49	206.2	16.838	9.473	9.474
1.39	191.0	16.706	9.544	9.545
1.29	176.5	16.661	9.614	9.615
1.19	161.6	16.666	9.690	9.690
1.10	147.4	16.718	9.766	9.767
1.03	135.0	16.833	9.837	9.837
0.957	123.5	17.001	9.906	9.907
0.886	112.0	17.208	9.980	9.981
0.807	98.98	17.477	10.071	10.072
0.710	83.22	17.834	10.194	10.195
0.613	67.31	18.151	10.337	10.338
0.530	53.40	18.346	10.484	10.484
0.460	41.09	18.489	10.638	10.639
0.409	31.61	18.632	10.783	10.784

**Table A.3.** continued.

$r - R_*$ [ $R_*$ ]	$v$ [ $\text{km s}^{-1}$ ]	$T_e$ [kK]	$\log n_{\text{tot}}$ [ $\text{cm}^{-3}$ ]	$\log n_e$ [ $\text{cm}^{-3}$ ]
0.377	25.42	18.792	10.897	10.898
0.350	20.20	18.968	11.014	11.015
0.324	15.31	19.179	11.152	11.152
0.305	11.83	19.379	11.276	11.277
0.289	9.120	19.569	11.400	11.401
0.271	6.478	19.779	11.561	11.562
0.254	4.382	19.981	11.742	11.743
0.240	3.034	20.169	11.912	11.912
0.229	2.158	20.393	12.067	12.068
0.220	1.569	20.693	12.213	12.213
0.212	1.167	21.069	12.347	12.348
0.204	0.8856	21.473	12.472	12.473
0.196	0.6579	22.015	12.607	12.608
0.185	0.4612	23.130	12.769	12.770
0.173	0.3227	24.656	12.933	12.934
0.160	0.2511	26.107	13.052	13.054
0.146	0.2198	27.468	13.121	13.126
0.128	0.1920	29.500	13.193	13.205
0.109	0.1482	32.389	13.320	13.342
0.886E-01	0.1047	35.787	13.487	13.520
0.690E-01	0.7372E-01	39.422	13.655	13.697
0.501E-01	0.5096E-01	43.149	13.831	13.877
0.324E-01	0.3425E-01	46.917	14.018	14.066
0.177E-01	0.2419E-01	50.535	14.182	14.230
0.777E-02	0.1890E-01	53.490	14.298	14.346
0.389E-02	0.1712E-01	54.771	14.344	14.392
0.194E-02	0.1629E-01	55.445	14.367	14.415
0.972E-03	0.1589E-01	55.797	14.379	14.427
0.00	0.1553E-01	56.141	14.390	14.438

**Table A.5.** Stratification for the atmosphere model with strong X-ray illumination ( $L_X \approx 10^{37}$  erg/s)

$r - R_*$ [ $R_*$ ]	$v$ [ $\text{km s}^{-1}$ ]	$T_e$ [kK]	$\log n_{\text{tot}}$ [ $\text{cm}^{-3}$ ]	$\log n_e$ [ $\text{cm}^{-3}$ ]
19.0	377.6	11.209	7.504	7.553
16.6	377.6	12.177	7.614	7.663
15.2	377.6	12.410	7.688	7.737
14.0	377.6	12.336	7.756	7.805
12.5	377.6	11.864	7.843	7.892
10.9	377.6	11.800	7.953	8.002
9.22	377.6	11.916	8.087	8.136
7.77	377.6	12.705	8.220	8.269
6.77	377.6	13.650	8.325	8.374
6.00	377.6	14.637	8.416	8.464
5.28	377.6	15.596	8.510	8.558
4.69	377.4	16.278	8.595	8.643
4.31	376.1	16.688	8.657	8.704
4.02	373.4	16.969	8.709	8.753
3.74	368.1	17.205	8.766	8.802
3.46	361.2	17.437	8.826	8.841
3.22	354.2	17.452	8.883	8.887
3.00	346.8	17.452	8.940	8.943
2.77	338.1	17.450	9.002	9.004
2.56	328.4	17.430	9.065	9.067
2.37	318.3	17.327	9.125	9.127
2.20	307.2	17.119	9.185	9.188
2.03	294.3	16.938	9.252	9.254
1.87	280.3	16.805	9.320	9.323
1.73	266.6	16.682	9.384	9.387

Table A.5. continued.

$r - R_*$ [ $R_*$ ]	$v$ [ $\text{km s}^{-1}$ ]	$T_e$ [kK]	$\log n_{\text{tot}}$ [ $\text{cm}^{-3}$ ]	$\log n_e$ [ $\text{cm}^{-3}$ ]
1.61	252.7	16.675	9.449	9.451
1.48	237.2	16.676	9.519	9.521
1.36	221.5	16.680	9.591	9.593
1.26	207.0	16.705	9.658	9.660
1.17	192.7	16.847	9.725	9.727
1.08	177.6	17.074	9.798	9.800
0.975	159.6	17.349	9.889	9.891
0.866	139.4	17.622	9.997	9.999
0.781	122.2	17.830	10.095	10.096
0.717	108.8	17.980	10.177	10.178
0.664	97.46	18.104	10.252	10.252
0.617	87.30	18.206	10.325	10.325
0.569	77.12	18.314	10.405	10.405
0.518	66.13	18.417	10.500	10.501
0.469	55.26	18.525	10.607	10.607
0.431	46.85	18.629	10.701	10.702
0.399	39.58	18.721	10.794	10.795
0.364	31.44	18.888	10.916	10.917
0.330	23.80	19.125	11.059	11.060
0.303	17.92	19.357	11.200	11.201
0.281	13.50	19.558	11.338	11.338
0.262	10.17	19.725	11.473	11.474
0.247	7.684	19.891	11.606	11.607
0.233	5.815	20.056	11.737	11.737
0.218	4.113	20.250	11.898	11.899
0.197	2.410	20.768	12.145	12.145
0.175	1.203	21.984	12.463	12.464
0.151	0.5996	23.922	12.783	12.785
0.129	0.3945	25.915	12.981	12.985
0.114	0.3283	27.535	13.073	13.079
0.103	0.2813	28.934	13.149	13.159
0.924E-01	0.2300	30.455	13.245	13.259
0.805E-01	0.1753	32.534	13.372	13.392
0.649E-01	0.1220	35.618	13.542	13.571
0.505E-01	0.8628E-01	38.818	13.704	13.742
0.411E-01	0.6676E-01	41.043	13.824	13.866
0.343E-01	0.5398E-01	42.704	13.922	13.967
0.281E-01	0.4344E-01	44.349	14.021	14.067
0.210E-01	0.3245E-01	46.373	14.154	14.201
0.127E-01	0.2287E-01	49.132	14.313	14.361
0.573E-02	0.1785E-01	51.904	14.426	14.474
0.286E-02	0.1663E-01	53.177	14.460	14.508
0.143E-02	0.1615E-01	53.832	14.474	14.522
0.716E-03	0.1592E-01	54.161	14.481	14.529
0.00	0.1569E-01	54.483	14.487	14.535